Received: 5 December 2017 | Revised: 12 March 2018 | Accepted: 23 April 2018

DOI: 10.4218/etrij.2017-0307

ORIGINAL ARTICLE

WILEY ETRI Journal

Implementation of cost-effective wireless photovoltaic monitoring module at panel level

Jin-Doo Jeong[1] | **Jinsoo Han**[1] | **Il-Woo Lee**[1] | **Jong-Wha Chong**[2]

[1]Hyper-connected Communication Research Laboratory, Electronics and Telecommunications Research Institute, Daejeon, Rep. of Korea.

[2]Department of Electronic Engineering, Hanyang University, Seoul, Rep. of Korea.

Correspondence
Jin-Doo Jeong, Hyper-connected Communication Research Laboratory, Electronics and Telecommunications Research Institute, Daejeon, Rep. of Korea.
Email: jdjeong@etri.re.kr

Funding information
Korea Institute of Energy Technology Evaluation and Planning (KETEP); Ministry of Trade, Industry & Energy (MOTIE) of the Republic of Korea, Grant/Award Number: 20173010013610

Given the rapidly increasing market penetration of photovoltaic (PV) systems in many fields, including construction and housing, the effective maintenance of PV systems through remote monitoring at the panel level has attracted attention to quickly detect faults that cause reductions in yearly PV energy production, and which can reduce the whole-life cost. A key point of PV monitoring at the panel level is cost-effectiveness, as the installation of the massive PV panels that comprise PV systems is showing rapid growth in the market. This paper proposes an implementation method that involves the use of a panel-level wireless PV monitoring module (WPMM), and which assesses the cost-effectiveness of this approach. To maximize the cost-effectiveness, the designed WPMM uses a voltage-divider scheme for voltage metering and a shunt-resistor scheme for current metering. In addition, the proposed method offsets the effect of element errors by extracting calibration parameters. Furthermore, a design method is presented for portable and user-friendly PV monitoring, and demonstration results using a commercial 30-kW PV system are described.

KEYWORDS
analog-to-digital conversion, calibration parameter, cost-effective, frequency shift keying, photovoltaic, shunt resistor, voltage/current metering, wireless MCU, wireless monitoring

1 | INTRODUCTION

The use of photovoltaic (PV) systems has increased rapidly in recent years owing to the steady reduction in PV module prices [1]. The global market deployment of PV technology experienced impressive growth and acceleration in 2015, and the globally installed total PV capacity is estimated at roughly 228 GW [2]. This rapid growth has led to the installation of numerous PV panels, including household PV systems for consumers, where the PV panels can be positioned on the rooftops of residential houses to minimize the amount of wasted space [3]. The huge expansion of the PV panel market can allow energy production to be as close as possible to the consumption nodes, thus shifting the dependence of energy resources for consumers from the electricity power grid to residential PV systems [3,4]. Accordingly, to reduce their whole-life costs and to mitigate the undesirable loss of PV power generation, the continuous monitoring of residential PV systems is important [5]. PV monitoring, particularly at the panel level, is attracting much attention because this approach allows for the quick detection of faults that cause reductions in PV energy production, while also enabling efficient maintenance processes [4,6].

Previous works on the monitoring of PV systems focused mainly on the monitoring of the overall behavior of PV systems or arrays [7–9]. However, recent studies have addressed PV monitoring at the panel level to achieve better reliability and efficiency of the PV system [4,10,11]. A key point is the cost-effectiveness in PV monitoring at the panel level owing to the vastly increased installation of PV

panels. One study [10] proposed a design method for panel-level monitoring modules using power line communication (PLC) considering its low cost. Wireless PV monitoring methods at the panel level have been proposed in several recent studies [4,11], with panel-level monitoring expanded to the diagnostics of PV systems. Voltage and current metering in one such study [4] are based on distributed maximum-power point architecture to conduct maximum-power point tracking (MPPT) at the panel level [12]. This method can increase the cost because individual panels need an additional microcontroller unit (MCU) for panel-level MPPT. Wireless PV monitoring methods [4,11] use 2.4-GHz wireless communications, where the path loss is considerable relative to that of sub-1-GHz communications. This occurs because the path loss in free space is proportional to the square of the frequency in those cases [13]. Thus, given the initial installation cost of wireless PV monitoring systems, the 2.4-GHz communications method is inferior to the sub-1-GHz case because monitoring systems using 2.4 GHz require more remote terminal units (RTUs) or gateways than in the case of sub-1-GHz communications. The IEEE 802.11 group, which standardizes wireless LAN systems at 2.4 GHz, is considering the sub-1-GHz band for several applications, such as advanced metering infrastructure (AMI) and distributed grid management [14].

In this paper, we propose an implementation method for a cost-effective wireless PV monitoring module (WPMM) at the panel level based on sub-1-GHz communication. The proposed WPMM measures the voltage and current, which is a mandatory step during PV monitoring, using cost-effective circuits. Metering degradation, which may occur because of the trade-off between cost and performance, is offset with calibration parameters. By employing the proposed design and compensation method, WPMM can maximize the level of cost-effectiveness.

The remainder of this paper is organized as follows. Section 2 describes the design concept of the WPMM implementation scheme. Then, Section 3 explains the design method of the WPMM, while Section 4 provides details about the parameter extraction method for metering calibration. Section 5 demonstrates the results of the implemented WPMM. Finally, Section 6 concludes the paper.

2 | CONCEPT OF WPMM IMPLEMENTATION

Figure 1 demonstrates the concept of a WPMM system. As shown in Figure 1, the WPMMs estimate the voltage and current of the PV panels, and transmit these estimated values to an RTU using a frequency-shift-keying (FSK) modulation scheme. FSK is an attractive communication scheme owing to its low complexity and low power consumption,

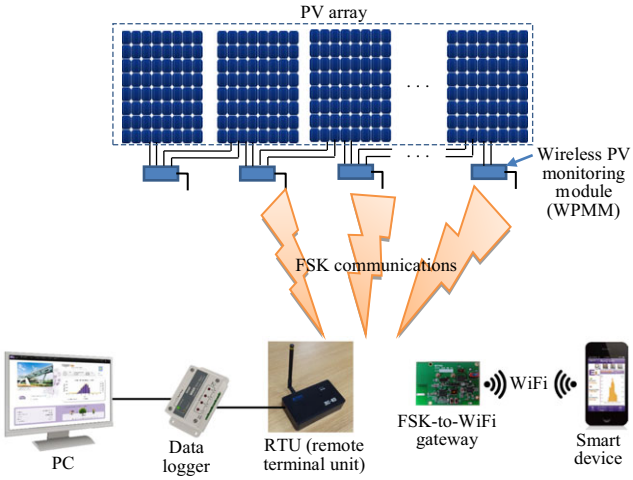

FIGURE 1 Demonstration of the concept of a wireless PV monitoring system

and it is widely used in applications that require long-range communication, such as smart utility networks (SUNs) and low-power wide-area networks (LPWANs) [15,16]. The PV data transmitted to the RTU are recorded at a data logger, and users can monitor the recorded PV data with a personal computer (PC). The PV data can also be given to users by employing a smart device using an FSK-to-Wi-Fi gateway, which converts data types from FSK to Wi-Fi, and vice versa. Users can conveniently use PV monitoring and management through a portable gateway and a smart device.

Figure 2 shows a conceptual diagram of the WPMM. The WPMM is composed of a power-generation module, current metering, voltage metering, and a wireless MCU for both analog-to-digital conversion (ADC) and FSK processing.

The WPMM obtains electric power from the PV panel. The voltage of the PV panel varies depending on factors such as the level of solar irradiation and the MPPT. The WPMM requires a stable and low-noise supply of power. Therefore, it is necessary that a stable voltage be obtained

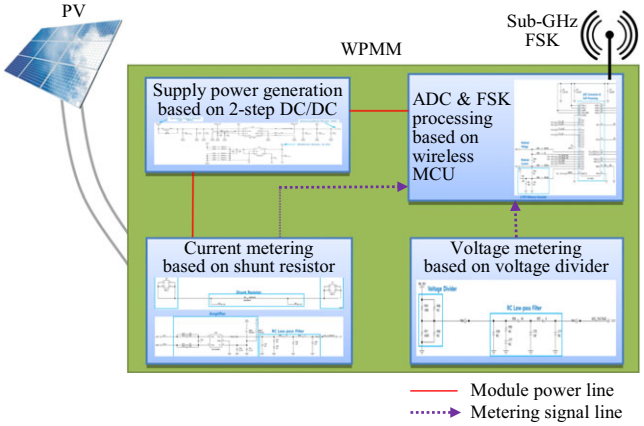

FIGURE 2 Conceptual diagram of the WPMM

despite the varying voltage of the PV panel. Considering this point, the WPMM adopts a two-step DC/DC conversion approach that is based on the intermediate voltage, similar to the intermediate frequency and is used to ensure stable operation in wireless radiofrequency (RF) systems. The next section presents the details of the power-generation process.

For cost-effective panel-level monitoring, voltage metering and current metering use a voltage divider and a shunt resistor, respectively. The voltage divider is composed of two resistors, as in an earlier study [17], and current metering typically utilizes one shunt resistor and one operational amplifier (OP-AMP), indicating that the voltage divider and the shunt resistor enable a cost-effective metering circuit. The next section also describes the details of the metering circuit.

Generally, an RF module and an MCU are used for wireless communication of the PV monitoring data and for control of the RF module, respectively. In this case, two chips are needed for wireless communication, which increases the cost. The proposed WPMM uses a wireless MCU to improve the cost-effectiveness, where the FSK modem and MCU are integrated.

3 | DESIGN OF THE WPMM

This section describes in detail the method used to design the WPMM.

3.1 | Generation of stable and low-noise power supply

Figure 3 shows a schematic diagram of the two-step DC/DC converter for a stable and low-noise power supply.

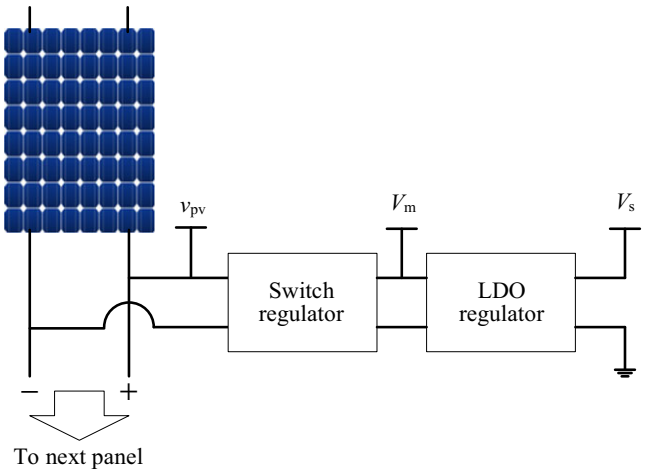

FIGURE 3 Schematic diagram of a two-step DC/DC conversion process

The voltage of the PV panel, the intermediate voltage, and the voltage of the wireless MCU are denoted as v_{pv}, V_m, and V_s, respectively. The PV voltage, v_{pv}, varies depending on the degree of solar irradiation. The practical PV panels used in this paper have voltage levels ranging from 0 V to 60 V. Both the OP-AMP and the wireless MCU use a 3.3-V voltage supply. The intermediate voltage V_m is adopted to compensate for conflicts between the variable panel voltage v_{pv} and the stable module voltage V_s.

A key point in the first step of the two-step DC/DC conversion process is the extraction of the intermediate voltage V_m near the module voltage V_s from the panel voltage v_{pv}. The WPMM uses a switching regulator that can have a large input range. However, the switching operation of the switching regulator usually causes noise. Thus, it is necessary to suppress the switching noise of the intermediate voltage V_m, to drop V_m down to V_s, and to stabilize V_s. In this study, a low-noise low-dropout (LDO) regulator was used in the second step for V_s. The intermediate voltage V_m was set to 5 V near the supply voltage V_s considering the conversion efficiency of the LDO regulator. This two-step conversion process ensures a stable and low-noise supply voltage from the variable and unstable voltage of the PV panel.

3.2 | Cost-effective voltage metering

The voltage metering circuit uses a voltage divider, as in a previous study [18], and is composed of several resistors, and can enable low-cost implementation. Figure 4 shows a schematic diagram of voltage metering at the panel level. In the figure, v_{pv}, R_1, R_2, and v_d represent the voltage of the PV panel, the resistance of the first resistor of the voltage divider, the resistance of the second resistor, and the divided voltage from the PV voltage v_{pv}, respectively. In addition, R_f and C_f denote the resistance of the resistor and the capacitance of the capacitor of the low-pass filter used. This low-pass filter suppresses high-frequency noise components out of the low-frequency band, where the slowly varying components of the voltage and current exist. The WPMM uses 0.001 as the time constant τ of the low-pass filter related to the cutoff frequency, as reported in a previous study [17].

From Figure 4, the divided voltage v_d can be expressed as (1) according to the principle of the voltage divider.

$$v_d = \frac{R_2}{R_1 + R_2} v_{pv} = \frac{1}{R_1/R_2 + 1} v_{pv}. \quad (1)$$

The divided voltage v_d is inputted to the ADC port in the wireless MCU in order to digitally measure the panel voltage, and wirelessly transfer it via the FSK communication channel. Thus, the relationship between the divided voltage v_d and the value measured through the ADC should be considered. The conversion range is an important factor associated with the ADC, and is the range of convertible

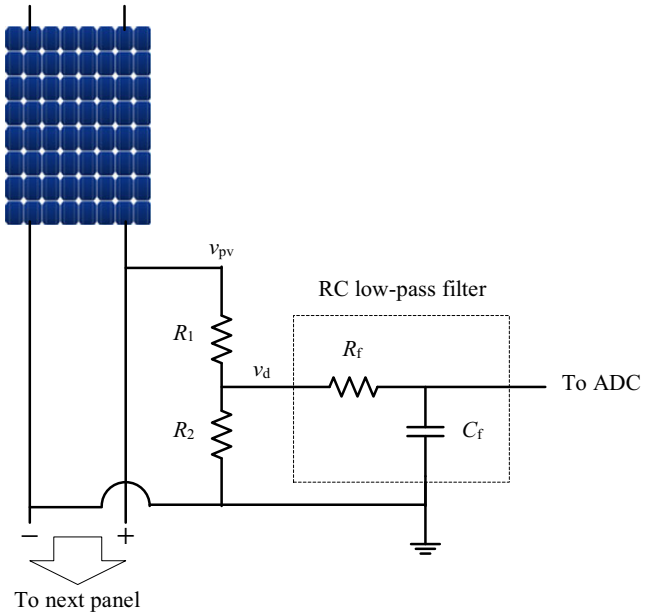

FIGURE 4 Schematic diagram of voltage metering at the panel level

input values. The single-ended ADC used in this study sets the conversion range using the reference voltage. In this case, the conversion range overlaps with the reference voltage. Considering the conversion range, it is best that the reference voltage of the ADC, denoted as V_{ADC}, be equal to the maximum divided voltage v_d, which is denoted by V_{d_max} and related to the maximum PV panel voltage v_{pv}. If V_{d_max} is larger than V_{ADC}, the divided voltage v_d larger than V_{ADC} is saturated to V_{ADC}, causing ADC distortion to occur. However, when V_{d_max} is smaller than V_{ADC}, the ADC quantization noise becomes larger because there is no conversion within the range of V_{d_max} to V_{ADC}. Accordingly, the ADC resolution is not fully used. These outcomes mean that the resistance ratio R_1/R_2 of the voltage divider in (1) should be set such that V_{d_max} is equal to or approaching V_{ADC}. For example, when $V_{ADC} = 2.5$ V, $R_1 = 10$ MΩ, and the maximum PV panel voltage, which is denoted by V_{pv_max}, is 60 V, (2) can be solved with $V_{d\_max} = V_{ADC}$ and using the results of (1).

$$V_{d\_max} = \frac{1}{R_1/R_2 + 1} \times 60 = V_{ADC} = 2.5. \quad (2)$$

By solving (2), the resistance ratio R_1/R_2 of the voltage divider in this example is 23.

The relationship between the divided voltage and the value measured through the ADC can be represented with a proportional expression because the voltage divider is composed of linear elements, such as a resistor. If V_{d_max} is equal to V_{ADC}, the relationship between the divided voltage v_d and the integer value, as measured through the ADC, adc_v, is expressed as follows:

$$v_d : adc_v = V_{ADC} : ADC_{max}. \quad (3)$$

In (3), ADC_{max} is the maximum integer outputted by the ADC, and is related to the resolution of the ADC. For an ADC with an 11-bit resolution, ADC_{max} is 2,047.

Equation (3) can be transformed as follows:

$$v_d = \frac{V_{ADC}}{ADC_{max}} adc_v. \quad (4)$$

By combining (1) and (4), the relationship between the PV panel voltage v_{pv} and the measured ADC value adc_v can be determined as follows:

$$v_{pv} = \left(\frac{R_1}{R_2} + 1\right) \frac{V_{ADC}}{ADC_{max}} adc_v. \quad (5)$$

Equation (5) shows that the PV panel voltage v_{pv} can be directly calculated using the ADC value adc_v that is measured or monitored at the MCU. In other words, the PV panel voltage can be simply obtained by applying the proportional constant $(R_1/R_2 + 1) \times V_{ADC}/ADC_{max}$ to the calculation program in the MCU.

3.3 | Cost-effective current metering

For cost-effectiveness, the current circuit uses a shunt resistor scheme composed of one shunt resistor and one amplifier, such as an OP-AMP [18]. Figure 5 illustrates a schematic diagram of current metering at the panel level. In the figure, R_s is the resistance of the shunt resistor, i_{pv} is the PV panel current passing through the shunt resistor, v_s is the voltage across the shunt resistor, G_a is the gain of the OP-AMP, and v_a is the voltage at the output of the OP-AMP. The time constant τ of the low-pass filter for noise suppression is set to 0.001, as in the voltage metering shown in Figure 4.

The amplified voltage v_a in Figure 5 can be represented as follows:

$$v_a = G_a v_s = G_a R_s i_{pv}. \quad (6)$$

Equation (6) shows that the PV panel current i_{pv} is proportional to the amplified voltage v_a with the proportional constant $G_a R_s$. As in voltage metering, the relationship between the amplified voltage v_a and the values measured through the ADC should be considered. Saturation occurs if the maximum amplified voltage, V_{a_max}, is greater than the ADC reference voltage V_{ADC}, whereas the quantization noise becomes larger if V_{a_max} is smaller than V_{ADC}. Considering the saturation and efficiency in the ADC, the proportional constant $G_a R_s$ in (6) should be adjusted properly such that V_{a_max} is equal to or approaches V_{ADC}. For example, when $V_{ADC} = 2.5$ V and the maximum of the PV panel current i_{pv} is 12.5 A, the desired $G_a R_s$ becomes 0.2.

The shunt resistor value should be carefully chosen considering the power rating in watts (W) relative to the

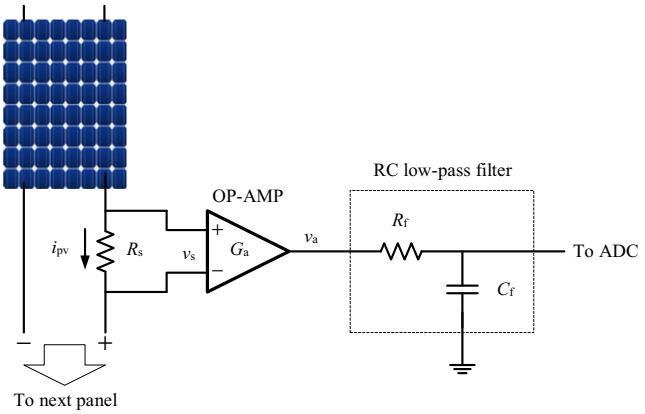

FIGURE 5 Schematic diagram of current metering at the panel level

maximum PV panel current i_{pv}. The relationship between the power p_s and current i_s at the shunt resistor is expressed using (7) with Ohm's law.

$$p_s = R_s i_s^2. \tag{7}$$

Shunt resistor manufacturers provide both resistance levels and power ratings, and thus both values are given. For convenience, when choosing a shunt resistor, (7) can be transformed as follows:

$$I_{s\_max} = \sqrt{P_r/R_s}. \tag{8}$$

In (8), P_r is the power rating of the shunt resistor, and I_{s_max} denotes the maximum current through the shunt resistor, which is calculated using the given values of P_r and R_s. The power rating of the shunt resistor can be considered by comparing the calculated I_{s_max} and the maximum current I_{pv_max} in the datasheet of the target PV panel. The maximum current I_{pv_max} of the PV panel should be greater than the calculated I_{s_max}.

If V_{a_max} is equal to V_{ADC}, similar to the case of voltage metering, the relationship between the amplified voltage v_a and the integer value measured through the ADC, adc_i, can be represented using a proportional expression, as follows:

$$v_a : adc_i = V_{ADC} : \mathrm{ADC}_{max}. \tag{9}$$

Equation (9) can be transformed as follows:

$$v_a = \frac{V_{ADC}}{\mathrm{ADC}_{max}} adc_i. \tag{10}$$

By combining (6) and (10), the relationship between the PV panel current i_{pvs} and the measured ADC value adc_v can be obtained as follows:

$$i_{pv} = \frac{1}{G_a R_s} \frac{V_{ADC}}{\mathrm{ADC}_{max}} adc_i. \tag{11}$$

As shown in (11), the PV panel current i_{pv} can be directly calculated with the ADC value adc_i. In other words, the PV panel current can be simply obtained by applying the proportional constant $1/G_a R_s \times V_{ADC}/\mathrm{ADC}_{max}$ to the calculation program in the MCU.

3.4 | Specifications of implemented WPMM

The specifications of the implemented WPMM are described in Table 1. In Table 1, V_{pv_max} and I_{pv_max} are determined according to the specification of the used PV panel, and the PV voltage range for the module operation represents the voltage range of the PV panel required to turn on the WPMM, which is dependent on the specifications of the designed power-generation scheme and the panel used. V_s and V_m are the parameters for the power-generation scheme designed in this paper, as described in Section 3.1, and the peak-to-peak supply voltage represents the peak-to-peak amplitude of the AC component of the module supply voltage, which is related to the magnitude of the noise of the DC supply voltage. The time constant τ and the cutoff frequency are the parameters of the used low-pass filter, and the resistance ratio R_1/R_2 is a parameter of the designed voltage-metering scheme, as described in Section 3.2. The ideal resistance ratio of the voltage divider is 23, as described in Section 3.2, but the resistance ratio is fitted to 23.2558, which is close to 23, owing to the difficulty achieving a combination of resistors for which the value is equal to 23. R_s, P_r, and G_a are parameters for the designed current metering scheme, as described in Section 3.3. In this study, a delta-sigma ADC was

TABLE 1 Specifications of the implemented WPMM

Maximum voltage of PV panel (V_{pv_max})	60 V
Maximum current of PV panel (I_{pv_max})	12.5 A
PV voltage range for module operation	4.5 V–60 V
Supply voltage of module (V_s)	3.3 V
Intermediate voltage for two-step DC/DC (V_m)	5 V
Peak-to-peak supply voltage	59.289 mV
Time constant τ of low-pass filter	0.001 s
Cutoff frequency of low-pass filter	159 Hz
Resistance ratio of voltage divider (R_1/R_2)	23.2558
Resistance of shunt resistor (R_s)	4 mΩ
Power rating of shunt resistor (P_r)	5 W
Gain of OP-AMP (G_a)	50
ADC scheme	Delta-Sigma
Number of used ADC ports	2
ADC reference voltage (V_{ADC})	2.5 V
ADC conversion range	0 V–2.5 V
ADC resolution	11 bit
ADC maximum output (ADC_{max})	2,047
Frequency band of wireless MCU	920 MHz
Modulation of wireless MCU	FSK

utilized as the ADC scheme, which is dependent on the specifications of the wireless MCU used, and the ADC used in this paper is robust to noise according to the properties of the delta-sigma ADC. V_{ADC} is used to determine the ADC conversion range is dependent on the parameters R_1/R_2, R_s, and G_a of the designed voltage and current schemes, as described in Sections 3.2 and 3.3. The ADC resolution and ADC_{max} are determined according to the specifications of the wireless MCU used. The frequency band and modulation of the wireless MCU, which represents the communication scheme used for wireless monitoring, are also determined according to the specifications of the wireless MCU used. The choice of the wireless MCU with a frequency band of 900 MHz means that the communication range is wider than those of communication schemes that utilize the 2.4-GHz frequency band. Moreover, the initial installation cost can be reduced owing to the requirement of fewer RTUs or gateways.

By applying the specifications in Table 1 to (5) and (11), the calculation equations for voltage metering and current metering are expressed as (12) and (13), respectively.

$$v_{pv} = 0.0296 \times adc_v, \tag{12}$$

$$i_{pv} = 0.0061 \times adc_i. \tag{13}$$

3.5 | Comparison between related works and the proposed WPMM

This section presents a comparison of existing wireless PV monitoring schemes that work at the panel level and the WPMM proposed in this paper. Table 2 shows the results of the comparison between the related works and the proposed WPMM.

From Table 2, voltage metering is generally performed using a voltage-divider scheme. Current metering in the work of Guerriero and others and in this paper is based on a shunt resistor, which can be composed of one OP-AMP and several passive circuit elements, such as a resistor and a capacitor, whereas the method reported by Caruso and others uses a commercial current sensor based on the Hall effect. In terms of cost efficiency, voltage and current metering using a voltage divider and a shunt resistor is advantageous because the metering circuit can consist of one OP-AMP and several low-cost passive circuit elements. Two ADC ports are typically used; thus, to calculate the voltage and current metering in the MCU, an ADC port is required for voltage and current metering. Therefore, it can be deduced that voltage and current metering are generally performed in a separate circuit. From a wireless communication perspective, the method proposed by Caruso and others and the WPMM use the sub-1-GHz frequency band, where the communication range is wider than 2.4 GHz [13], whereas other methods use the 2.4-GHz frequency band. In addition, the method proposed by Caruso and others uses a commercial communication module that is based on an amplitude shift keying (ASK) scheme, with the performance degraded to a greater extent relative to that of the FSK scheme [20]. This implies that the proposed WPMM can handle long-range communication compared to other methods, and that the initial installation cost can be reduced owing to the smaller number of RTUs or gateways that are required. From Table 2, when calculating the metering values using the MCU, the calculation process employed by the MCU includes steps that incorporate the ADC parameters. These steps that consider the ADC parameters are described only in our paper, and to the best of our knowledge, the consideration of the ADC parameters has not been proposed in other studies.

In summary, the WPMM design method proposed in this paper is more cost-effective compared to the previous works because the low complexity of the metering circuit is obtained by using the voltage divider and shunt resistor schemes. In addition, in terms of installation cost, the installation efficiency of the RTUs communicating with the WPMMs is enhanced owing to the wide communication range and the robust communication performance that are obtained by using the FSK in the sub-1-GHz frequency band.

4 | PARAMETER EXTRACTION FOR METERING CALIBRATION AND ACCURACY ANALYSIS OF THE WPMM METERING

This section proposes a parameter-extraction method that compensates the metering deviation owing to the errors of

TABLE 2 Comparison of the related works and the proposed WPMM

Authors [Ref]	Ando et al. [4]	Guerriero et al. [11]	Caruso et al. [17]	Rashidi et al. [19]	Proposed WPMM
Voltage metering	Using commercial module	Voltage divider	Voltage divider	Not described	Voltage divider
Current metering		Shunt resistor	Hall effect		Shunt resistor
Number of ADC ports	Not described	2	2	2	2
Consideration of ADC parameters	No	No	No	No	Yes
Communication scheme	FSK	IEEE 802.15.4	ASK	IEEE 802.15.4	FSK
Frequency band (GHz)	2.4	2.4	0.315	2.4	0.92

practical circuit elements, and analyzes the metering accuracy of the WPMM previously proposed in Section 3. In addition, the measurement and calibration of the PV temperature are described in connection with the proposed methods.

4.1 | Parameter extraction for metering calibration

The voltage and current of the PV panel can be calculated with values measured by employing the ADC using the linear equations shown in (5) and (11). This is because the voltage and current circuits are composed of linear elements such as resistors and amplifiers. For simplicity, (5) and (11) are converted to (14) and (15), respectively.

$$v_{\mathrm{pv}} = K_v \cdot adc_v \text{ where } K_v = \left(\frac{R_1}{R_2} + 1\right) \frac{V_{\mathrm{ADC}}}{\mathrm{ADC}_{\mathrm{max}}}, \quad (14)$$

$$i_{\mathrm{pv}} = K_i \cdot adc_i \text{ where } K_i = \frac{1}{G_a R_s} \frac{V_{\mathrm{ADC}}}{\mathrm{ADC}_{\mathrm{max}}}. \quad (15)$$

In (14) and (15), K_v and K_i are the proportional constants for voltage metering and current metering, respectively. However, for the expressions in (14) and (15) to be valid, it is assumed that the elements used are ideal, whereas electronic devices typically have errors. The resistance of a practical resistor may deviate from the designated resistance, and the possible error range, known as the tolerance, is provided. Gain deviation is also possible in practical OP-AMPs. Thus, the expressions in (14) and (15) should be modified to compensate for error effects to enable more accurate metering. When variables that reflect the effects of errors are applied, (14) and (15) can be, respectively, modified to become (16) and (17).

$$v_{\mathrm{pv}} = (K_v + \Delta_{v\_s}) \cdot adc_v + \Delta_{v\_y}, \quad (16)$$

$$i_{\mathrm{pv}} = (\mathrm{K}_i + \Delta_{i\_s}) \cdot adc_i + \Delta_{i\_y}. \quad (17)$$

In (16), Δ_{v_s} and Δ_{v_y} represent the deviation of the slope and the deviation of the y-intercept caused by errors in the elements for voltage metering, respectively. In (17), Δ_{i_s} and Δ_{i_y}, respectively, denote the deviation of the slope and the deviation of the y-intercept caused by errors in the elements for current metering. The deviations Δ_{v_s}, Δ_{v_y}, Δ_{i_s}, and Δ_{i_y} can be utilized as parameters for calibrating the WPMM. The calibration parameters in each WPMM are different from each other because the element errors are all different in each WPMM. This means that the calibration parameters of each WPMM should be extracted by performing experiments. Figure 6 shows the experimental environment used to extract the calibration parameters.

In Figure 6, the power supply functions as a virtual PV to supply power to the WPMM, and as a voltage controller to adjust the voltage to the WPMM. Moreover, the currents are controlled by the DC electronic load. The voltage and current, which are maintained at specified values, as well as the peak-to-peak supply voltage are monitored using an oscilloscope. Values measured through the ADC in the wireless MCU can be monitored with a PC.

In this paper, an inverse function was used to obtain the calibration parameters. A specified value for voltage or current is inputted to the WPMM, and the ADC value that matches the specified value is monitored. Subsequently, a linear function is obtained using the voltage or current as a variable. Finally, the inverse function of the obtained linear function is calculated. The calibration parameters are then extracted from (16), (17), and the inverse function. To verify these processes of extracting the calibration parameters, linear functions with voltage and current variables are set, as in (18) and (19), respectively.

$$adc_{v\_\mathrm{m}} = S_v \cdot v_{\mathrm{sp}} + Y_v, \quad (18)$$

$$adc_{i\_\mathrm{m}} = S_i \cdot i_{\mathrm{sp}} + Y_i. \quad (19)$$

In (18), adc_{v_m} is the ADC value for the voltage monitored with a PC, v_{sp} is the voltage set to a specified value, S_v is the slope of the linear function with the voltage variable, and Y_v is the y-intercept of the linear function with the voltage variable. Similarly, in (19), adc_{i_m} is the ADC value for current monitored with a PC, i_{sp} is the current set to a specified value, S_i is the slope of the linear function with the current variable, and Y_i is the y-intercept of the linear function with the current variable. Constant values S_v, Y_v, S_i, and Y_i in (18) and (19) can be determined by performing the experiment described above. The inverse functions of (18) and (19) are respectively calculated using (20) and (21).

$$v_{\mathrm{sp}} = 1/S_v \cdot adc_{v\_\mathrm{m}} - Y_v/S_v, \quad (20)$$

$$i_{\mathrm{sp}} = 1/S_i \cdot adc_{i\_\mathrm{m}} - Y_i/S_i. \quad (21)$$

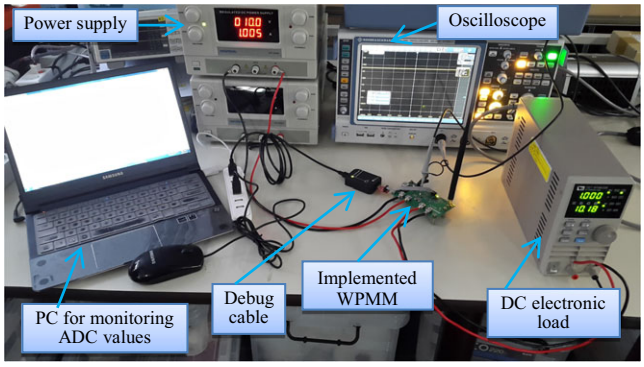

FIGURE 6 Experiment environment for obtaining the calibration parameters

Because the experimental environment considers all practical cases, it is reasonable that $v_{pv} = v_{sp}$, $i_{pv} = i_{sp}$, $adc_v = adc_{v\_m}$, and $adc_i = adc_{i\_m}$. Therefore, the calibration parameters can be obtained as in (22) and (23) using (16), (17), (20), and (21).

$$\Delta_{v\_s} = 1/S_v - K_v, \Delta_{v\_y} = -Y_v/S_v, \tag{22}$$

$$\Delta_{i\_s} = 1/S_i - K_i, \Delta_{i\_y} = -Y_i/S_i. \tag{23}$$

Figure 7 presents an example of the determination of the calibration parameters for the implemented WPMM. As described in the previous section, for the implemented WPMM with the specifications presented in Table 1, K_v and K_i are 0.0296 and 0.061, respectively. Figure 7A is related to (18) and (19), and is used to obtain linear functions experimentally, Figure 7B is related to (20) and (21), and is used to calculate the inverse functions from the obtained linear functions, and Figure 7C presents metering equations with the extracted calibration parameters related to (16) and (17).

Table 3 presents the calibration parameters that were obtained for the 12 implemented WPMMs. As shown in the table, the effects of element errors appear to be minor, and metering approximation is possible using (5) and (11), including only design specifications, whereas precise metering can be achieved with the calibration parameters in Table 3.

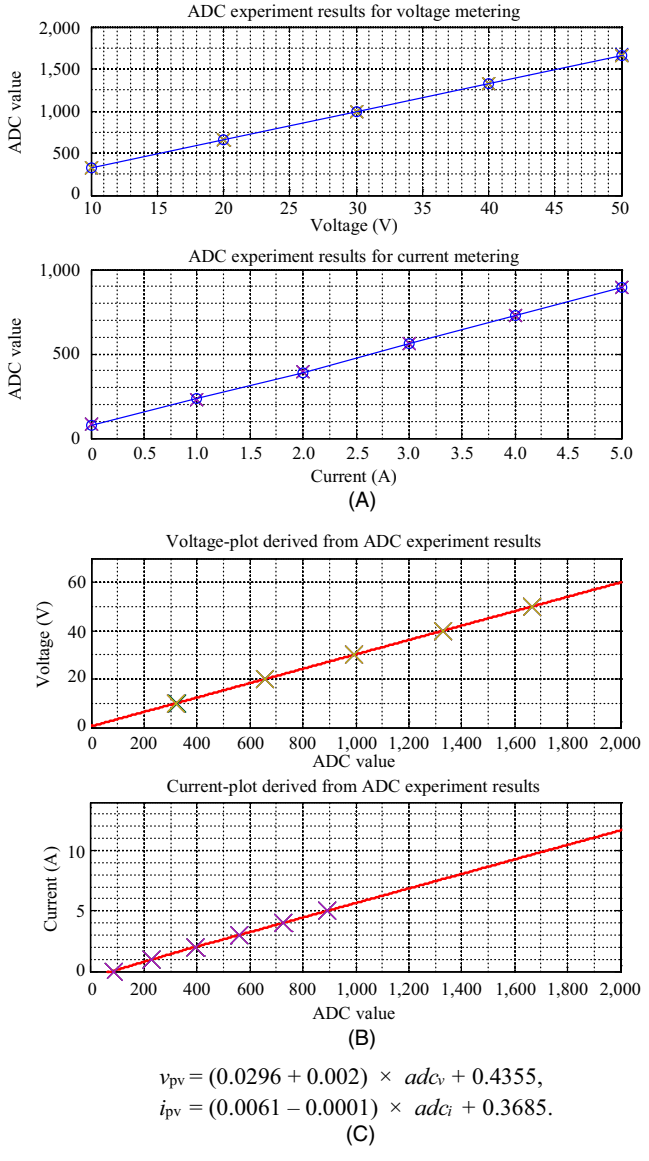

FIGURE 7 Example of the extraction of calibration parameters: (A) linear functions obtained experimentally, (B) inverse functions calculated from the obtained linear functions, and (C) metering equations with the obtained calibration parameters

4.2 | Accuracy analysis of the WPMM metering

In the previous subsection, the parameter-extraction method has been proposed to compensate for the metering deviation owing to the errors of the practical circuit elements. Here, the importance of the parameter extraction is discussed by analyzing the accuracy of the voltage metering and the current metering of the proposed WPMM.

The absolute error of the WPMM metering can be set to deviate from the precise metering value, which is calibrated using the parameter extraction method, and can be represented as (24) and (25) for the voltage metering and the current metering, respectively, using (14), (15), (16), and (17).

$$\begin{aligned}\varepsilon_v &= \left|[K_v \cdot adc_v] - \left[(K_v + \Delta_{v\_s}) \cdot adc_v + \Delta_{v\_y}\right]\right| \\ &= \left|\Delta_{v\_s} \cdot adc_v + \Delta_{v\_y}\right|,\end{aligned} \tag{24}$$

TABLE 3 Calibration parameters obtained for the 12 implemented WPMMs

Index of WPMMs	Δ_{v_s}	Δ_{v_y}	Δ_{i_s}	Δ_{i_y}
1	0.0002	0.4355	−0.0001	−0.3685
2	0.0001	0.1959	−0.0001	−0.096
3	0.0001	0.4458	−0.0001	0.0127
4	0.0001	0.3423	−0.0001	−0.0039
5	−0.0001	0.3451	−0.0001	0.016
6	0.0001	0.2615	−0.0001	0.0611
7	−0.0001	0.3542	−0.0001	0.0903
8	0	0.3872	−0.0001	−0.1104
9	0	0.3973	−0.0001	−0.0357
10	−0.0001	0.4113	−0.0002	0.2393
11	0.0002	0.2084	−0.0001	−0.1439
12	0.0003	0.3933	−0.0001	0.0356

$$\begin{aligned}\varepsilon_i &= \left|[\mathrm{K}_i \cdot adc_i] - \left[(K_i + \Delta_{i\_\mathrm{s}}) \cdot adc_i + \Delta_{i\_\mathrm{y}}\right]\right| \\ &= \left|\Delta_{i\_\mathrm{s}} \cdot adc_i + \Delta_{i\_\mathrm{y}}\right|.\end{aligned} \tag{25}$$

In (24) and (25), ε_v and ε_i are the errors for the voltage metering and the current metering, respectively. The first terms in (24) and (25) are proportional to the ADC outputs adc_v and adc_i, whereas the second terms are constant. This means that the effect of the first term on the metering error may dominate the second term in the case of an ADC with high resolution. In the cases of (24) and (25), the maximum metering error values are obtained when the respective ADC outputs, adc_v and adc_i, are equal to zero or the maximum value $\mathrm{ADC}_{\max}$. Therefore, error bounds for the voltage metering and the current metering can be expressed as (26) and (27), where max{} selects the maximum from among the arguments in the curly brackets.

$$\varepsilon_v \le \max\left\{\left|\Delta_{v\_\mathrm{s}} \cdot \mathrm{ADC}_{\max} + \Delta_{v\_\mathrm{y}}\right|, \left|\Delta_{v\_\mathrm{y}}\right|\right\}, \tag{26}$$

$$\varepsilon_i \le \max\left\{\left|\Delta_{i\_\mathrm{s}} \cdot \mathrm{ADC}_{\max} + \Delta_{i\_\mathrm{y}}\right|, \left|\Delta_{i\_\mathrm{y}}\right|\right\}. \tag{27}$$

Table 4 shows the absolute maximum values of the metering errors ε_v and ε_i that are due to the errors of the practical circuit elements used to implement the 12 WPMMs with the specifications in subsection 3.4 and the calibration parameters in subsection 4.1. For the metering error bounds in (26) and (27), this paper does not consider the errors owing to the imprecision of the experimental equipment used in the parameter-extraction process because the errors in the experimental equipment are relatively small, and are generally negligible.

TABLE 4 Absolute maximum of the metering errors ε_v and ε_i due to the errors of the practical circuit elements used to implement the 12 WPMMs

Index of WPMMs	Absolute maximum of ε_v	Absolute maximum of ε_i
1	0.8449	0.5732
2	0.4006	0.3007
3	0.6505	0.1920
4	0.5470	0.2086
5	0.3451	0.1887
6	0.4662	0.1436
7	0.3542	0.1144
8	0.3872	0.3151
9	0.3973	0.2404
10	0.4113	0.6487
11	0.6178	0.3486
12	1.0074	0.2403

Table 4 shows the maximum of the absolute maxima for the voltage metering error ε_v, in the 12th WPMM, and the maximum occurs in the 10th WPMM for the current-metering error ε_i. For both of the cases, the slopes have absolute maximum values of Δ_{v_s} and Δ_{i_s}. These demonstrate that the metering errors are more affected by the first terms with the proportionality in (24) and (25), as described in the previous paragraph.

The metering errors in (26) and (27) are represented when the design method in section 3 is only applied and the calibration process in subsection 4.1 is not performed. In other words, the metering error bounds in Table 4 can be reduced by obtaining the parameters for the metering calibration. Accordingly, it can be stated that the PV monitoring system that is implemented with the design and the calibration methods proposed in this paper have greater accuracy compared to other systems with no calibration.

4.3 | Measurement and calibration of PV temperature

The temperature of the PV module affects the PV module power and the current-voltage characteristics, which is also called an IV curve, and the PV temperature is a factor that is measured when monitoring the PV module. In [4], TMP36 was used as the temperature sensor to monitor the PV at the panel level. Temperature sensors, including TMP36, normally output analog voltage values that are proportional to the temperature, and the proportional constant between the temperature and the analog voltage is also referred to as a scale factor [21]. Therefore, the temperature can be measured in the MCU by using the scale factor proportional to the analog voltage of the temperature sensor and a port of the ADCs of the MCU, taking the analog voltage as the ADC input. This means that the measurement of the temperature can be performed using a similar method in the voltage metering or the current metering, as described in Section 3. Thus, the mathematical representation for measuring the temperature can be as in (28), which is similar to (14) or (15).

$$T_{\mathrm{pv}} = K_T \cdot adc_T + T_{\mathrm{o}}. \tag{28}$$

In (28), T_{pv} is the PV temperature, adc_T is the ADC output, which takes the analog voltage of the temperature sensor as the input, K_T is the proportional coefficient, and To is the temperature offset. The proportional coefficient K_T and the temperature offset To can be obtained using the specification of the used ADC, including the ADC resolution and the specification of the used temperature sensor including the scale factor,

the output voltage range, and the output voltages at the specific temperatures.

There is an uncertainty regarding the temperature measured using (28) because of the accuracy of the temperature sensor and the quantization error of the ADC [4]. This means that a more accurate calibration process is required for the temperature measurement. The calibration process for the temperature measurement can be performed using a method that is similar to obtaining the parameters for the voltage metering or the current metering. The mathematical representation of the parameter extraction for the calibration of the temperature measurement can be as given in (29), which is similar to (16) or (17).

$$T_{\mathrm{pv}} = (K_T + \Delta_{T\_s}) \cdot adc_T + \left(T_{\mathrm{o}} + \Delta_{T\_y}\right). \tag{29}$$

In (29), Δ_{T_s} and Δ_{T_y} represent the deviation of the slope and the deviation of the y-intercept caused by uncertainties that result from the accuracy of the temperature sensor and the quantization error of the ADC, respectively. The calibration parameters Δ_{T_s} and Δ_{T_y} can be obtained experimentally using a process that is similar to that described in the subsection 4.1. The accuracy of the temperature measurement can be improved by obtaining the calibration parameters, and may be superior to the accuracy described in the data sheet of the used temperature sensor.

5 | DEMONSTRATION OF IMPLEMENTED WPMMS

To verify the PV monitoring function using the implemented WPMMs, demonstration results that were obtained when applying the WPMMs to a commercial PV are presented in this section. Before the demonstration results, a gateway for user-friendly PV monitoring through a smart device is described.

5.1 | Design of gateway for user-friendly PV monitoring

As shown in Figure 1, the implementation of PV monitoring is normally done using an RTU, a data logger, and a PC. This monitoring method limits the user's convenience on the move. This limitation in terms of the movement can be overcome by using a portable smart device. However, smart devices do not support any FSK modulation appropriate for long-range communication. Thus, a user-friendly gateway that converts FSK data to Wi-Fi data is needed.

Figure 8 presents a conceptual diagram of a gateway for user-friendly PV monitoring. The WPMM transfers the metered data through the FSK, whereas smart devices generally include a Wi-Fi communication module. Thus, the gateway for user-friendly PV monitoring plays the role of a bridge to transfer the data received through the FSK to a smart device using Wi-Fi communication, and vice versa. The gateway transfers data through a universal asynchronous receiver/transmitter (UART) that is similar to the type widely used in MCUs.

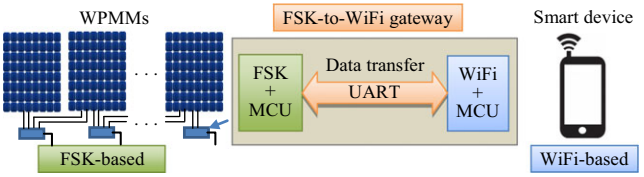

FIGURE 8 Conceptual diagram of a gateway for user-friendly PV monitoring

The process that is employed to transmit PV metering data between each PV module, the FSK gateway, and a smart device can be explained as follows. First, the voltage and the current data of each PV module, which are metered using the methods described in Sections 3 and 4, are transmitted wirelessly to the FSK gateway through the FSK-modulated signals. Next, the PV metering data are transferred to the Wi-Fi module in the FSK gateway through the UART, and then the Wi-Fi signals, including the PV metering data, are generated by the Wi-Fi module to transmit the PV metering data via a Wi-Fi communication link, which is normally provided by portable smart devices. Finally, the smart device receiving the Wi-Fi signals displays the PV metering data using a graphical user interface (GUI) that supports the Wi-Fi socket communication. The Wi-Fi socket communication is programmed differentially according to the operating system (OS) of a smart device, such as Android and IOS. In this study, the GUI developed to support the Wi-Fi socket communication and to display of the PV metering information were programmed using the Android OS, as described in the following section.

5.2 | Demonstration results for implemented WPMMs

The 12 implemented WPMMs were demonstrated using a commercial PV array. First, the 12 implemented WPMMs were installed into the array of a 30-kW commercial PV system. Figure 9 shows the WPMMs installed in the actual PV system. The 12 installed WPMMs perform wireless monitoring of one string composed of 12 practical panels. As shown in Figure 9, the WPMMs are installed on the PV panel support separately from the

FIGURE. 9 (A) 12 WPMMs installed to a practical 30 kW PV system and (B) close-up view of Figure 9A

junction box. This installation method can take advantage of the fact that WPMMs can be easily installed in existing PV systems that are composed of conventional PV panels.

Figure 10 shows the PV monitoring results of the WPMM and the gateway. Figure 10A shows the PV monitoring results that were obtained using a GUI, which depicts the monitoring data transferred through the RTU and the data logger. Figure 10B shows the user-friendly PV monitoring results that were obtained using a consumer device and the portable gateway designed in this paper. From Figure 10, the WPMM and gateway implemented in this paper can realize continuous panel-level PV monitoring, which allows the rapid detection of faults that may affect PV energy production and that reduce the whole-life cost when using consumer devices. Therefore, it can be deduced that the implemented WPMM and gateway are suitable for residential PV systems, which are currently being widely implemented as consumer applications.

6 | CONCLUSION

In this paper, we proposed a method for the implementation of a cost-effective WPMM that works at the panel level. Panel-level PV monitoring can enhance the management efficiency of PV systems, although it requires the installation of a large number of

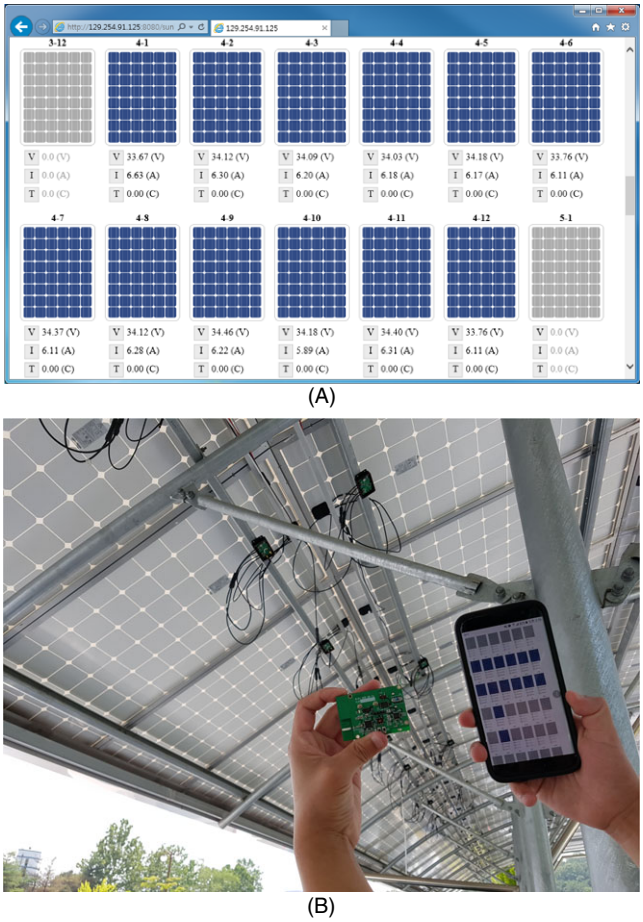

FIGURE 10 PV monitoring results obtained using the implemented WPMMs and gateway: (A) RTU, a data logger, and PC and (B) smart device and the implemented gateway

monitoring modules. Along with the rapid market penetration of PV systems, this paper highlights the cost-effectiveness of PV monitoring at the panel level. The implemented WPMM is composed of voltage metering based on a voltage divider with two resistors, current metering based on a shunt resistor scheme with one shunt resister and one OP-AMP, and a wireless MCU that integrates an FSK modem and an MCU on a single chip. Thus, the WPMM is considered to be cost-effective. More accurate metering can be realized with the proposed extraction of calibration parameters, which compensate for the effect of element errors. In addition, a gateway for user-friendly PV monitoring was implemented. The PV monitoring function of the WPMM and the gateway were verified by performing a demonstration using an actual PV array. Panel-level PV monitoring using the proposed cost-effective WPMMs can reduce not only the initial installation cost but also the operation cost owing to the ability to realize efficient management of the PV system. Therefore, to improve the PV management

efficiency, based on the results in this study, further research can focus on PV diagnostics technology to address issues such as degradation and faults based on the proposed WPMM.

ACKNOWLEDGMENTS

This work was supported by the Korea Institute of Energy Technology Evaluation and Planning (KETEP) and the Ministry of Trade, Industry & Energy (MOTIE) of the Republic of Korea (No. 20173010013610).

ORCID

Jin-Doo Jeong http://orcid.org/0000-0002-8137-1502

REFERENCES

1. B. Burger et al., Photovoltaics report, Fraunhofer ISE, Freiburg, Germany, Nov. 2016. https://www.ise.fraunhofer.de/content/dam/ise/de/documents/publications/studies/Photovoltaics-Report.pdf
2. S. Nowak, *Trends 2016 in Photovoltaic applications: Survey report of selected IEA countries between 1992 and 2015*, Report IEA-PVPS T1-30:2016, 2016. http://www.iea-pvps.org/fileadmin/dam/public/report/national/Trends_2016_-_mr.pdf
3. B. Lee et al., *Degradation diagnosis system of photovoltaic panels with mobile application*, IEEE Trans. Consum. Electron. **60** (2014), no. 3, 338–346.
4. B. Ando et al., *Sentinella: Smart monitoring of photovoltaic systems at panel level*, IEEE Trans. Instrum. Meas. **64** (2015), no. 8, 2188–2199.
5. T. Mukai et al., *The competitiveness of continuous monitoring of residential PV systems: A model and insights from the Japanese market*, IEEE Trans. Sustain. Energy **5** (2014) no. 4, 1176–1183.
6. J. Han et al., *PCL-based photovoltaic system management for smart home energy management system*, IEEE Trans. Consum. Electron. **60** (2014), no. 2, 184–189.
7. M. Davarifar et al., *Real-time model base fault diagnosis of PV panels using statistical signal processing*, Proc. Int. Conf. Renew. Energy Res. Appl. (ICRERA), Madrid, Spain, Oct. 2013, pp. 599–604.
8. M. Benghanem and A. Maafi, *Data acquisition system for photovoltaic systems performance monitoring*, IEEE Trans. Instrum. Meas. **47** (1998), no. 1, 30–33.
9. A. Carullo et al., *In situ calibration of heterogeneous acquisition systems: The monitoring system of a photovoltaic plant*, IEEE Trans. Instrum. Meas. **59** (2010), no. 5, 1098–1103.
10. J. Han, I. Lee, and S.-H. Kim, *User-friendly monitoring system for residential PV system based on low-cost power line communication*, IEEE Trans. Consum. Electron. **61** (2015) no. 2, 175–180.
11. P. Guerriero et al., *Monitoring and diagnostics of PV plants by a wireless self-powered sensor for individual panels*, IEEE J. Photovolt. **6** (2016), no. 1, 286–294.
12. Y.-M. Chen, C.-W. Chen, and Y.-L. Chen, Development of an autonomous distributed maximum power point tracking PV system, *IEEE Proc. Energy Convers. Congr. Expo. (ECCE)*, Phoenix, AZ, USA, Sept. 2011, pp. 3614–3619.
13. L. C. Fernandes and A. J. M. Soares, *Simplified characterization of the urban propagation environment for path loss calculation*, IEEE Antennas Wireless Propag. Lett. **9** (2010), 24–27.
14. S. Aust and T. Ito, Sub 1 GHz wireless LAN propagation path loss models for urban smart grid applications, *Proc. Int. Conf. Comput. Netw. Commun. (ICNC)*, Maui, HI, USA, Jan. 30–Feb. 2, 2012, pp. 116–120.
15. M. K. Oh et al., *A fully integrated IEEE 802.15.4g MR-FSK SoC for smart utility network applications*, IEEE Trans. Consum. Electron. **60** (2014), no. 4, 580–586.
16. X. Xiong et al. *Chatzimisios, low power wide area machine-to-machine networks: Key techniques and prototype*, IEEE Commun. Mag. **53** (2015), no. 9, 64–71.
17. M. Caruso et al., A low-cost, real-time monitoring system for PV plants based on ATmega 328P-PU microcontroller, *Proc. IEEE Inf. Telecommun. Energy Conf. (INTELEC)*, Osaka, Japan, Oct. 18–22, 2015, pp. 1–5.
18. Texas Instruments, *LMP8645HV precision high voltage current sense amplifier*, Texas Instruments, LMP8645, Texas, USA, Sept. 2015. http://www.ti.com/lit/ds/symlink/lmp8645.pdf
19. Y. Rashidi, M. Moallem, and S. Vojdani, Wireless Zigbee system for performance monitoring of photovoltaic panels, *IEEE Photovolt. Specialists Conf. (PVSC)*, Seattle, WA, USA, June 19–24, 2011, pp. 3205–3207.
20. J. G. Proakis, *Optimum receivers for the additive white Gaussian noise channel*, *Digital Communications*, 4th ed, McGraw-Hill, New York, USA, 2001, pp. 231–318.
21. Analog Device, TMP35/TMP36/TMP37 Data Sheet, Low Voltage Temperature Sensors, Analog Device, MA, USA. http://www.analog.com/media/en/technical-documentation/data-sheets/TMP35_36_37.pdf

AUTHOR BIOGRAPHIES

Jin-Doo Jeong received his BS degree in electronic engineering in 1998, and his MS and PhD degrees in electronic and communication engineering in 2000 and 2017, respectively, from Hanyang University, Seoul, Rep. of Korea. In 2010, he joined the Electronics and Telecommunications Research Institute (ETRI), Daejeon, Rep. of Korea, where he has worked on wireless personal area communication systems using UWB and VLC. He is a senior researcher in ETRI, and his research focus is in the area of energy IT technology, including smart metering, wireless energy management, and photovoltaic system operations and maintenance.

Jinsoo Han received his BS degree in electronics engineering from Yonsei University in Seoul, Rep. of Korea., in 1998, and the MS degree in electrical and electronics engineering from KAIST in Daejeon, Rep. of Korea., in 2000. He is a PhD candidate at Chungnam National University, Daejeon, Rep. of Korea. He joined the Electronics and Telecommunications Research Institute (ETRI), Daejeon, Rep. of Korea, in 2000. At ETRI, he was involved in the development of optical communication systems and optical networks. He has also been engaged in the research and development of home gateway and home server systems, wired and wireless home networks, and power management systems. His current research interests are wireless sensor networks (WSNs), home/building energy management, and green IT solutions.

Il-Woo Lee received the BS and MS degrees in computer science from Kyung Hee University, Seoul, Rep. of Korea, in 1992 and 1994, respectively, and the PhD degree in computer science from Chungnam National University, Daejeon, Rep. of Korea, in 2007. He joined the Electronics and Telecommunications Research Institute, Daejeon, Rep. of Korea. in 1994, and has been engaged in the research and development of CDMA, TDX-10 ISDN, high-speed routing systems, and home network systems, etc. He is currently a director of the energy IT technology research section, and his research interests are smart grid/microgrid platforms, DER, energy trading, and energy informatics.

Jong-Wha Chong received his BS and MS degrees in electronics engineering from Hanyang University, Seoul, Rep. of Korea, in 1975 and 1979, respectively, and a PhD degree in electronics and communication engineering from Waseda University, Tokyo, Japan, in 1981. Since 1981, he has been with the Department of Electronics Engineering at Hanyang University, where he is now a chair professor. From 1979 to 1980, he was a researcher at the C&C Research Center of Nippon Electronic Company, Tokyo, Japan. From 1983 to 1984, he was a visiting researcher at the Korean Institute of Electronics & Technology, Seongnam, Rep. of Korea. In 1986 and 2008, he was a visiting professor at the University of California, Berkeley, USA. He was the chairman of the CAD & VLSI society of the Institute of the Electronic Engineers of Korea in 1993, and the president of the IEEK and of the KIEEE in 2007, and from 2009 to 2010, respectively. His current research interests are SoC design methodology (including memory centric design and physical design automation of 3D ICs); indoor wireless communication SoC design for ranging and location; video systems; and power IT systems.